Computer Methods and Programs in Biomedicine 256 (2024) 108375

Contents lists available at ScienceDirect

Computer Methods and Programs in Biomedicine

journal homepage: https://www.sciencedirect.com/journal/computer-methods-and-programs-in-biomedicine

Physically informed deep neural networks for metabolite-corrected plasma input function estimation in dynamic PET imaging

Matteo Ferrante [a,*], Marianna Inglese [a], Ludovica Brusaferri [b,c], Alexander C. Whitehead [d], Lucia Maccioni [e], Federico E. Turkheimer [f], Maria A. Nettis [g], Valeria Mondelli [g], Oliver Howes [h], Marco L. Loggia [b,i], Mattia Veronese [e], Nicola Toschi [a,b]

[a] Department of Biomedicine and Prevention, University of Rome, Tor Vergata, Rome, Italy
[b] Athinoula A. Martinos Center For Biomedical Imaging, MGH and Harvard Medical School, Boston, MA, USA
[c] Department of Computer Science and Informatics, School of Engineering, London South Bank University, London, UK
[d] Department of Computer Science, University College London, London, UK
[e] Department of Information Engineering, University of Padua, Padua, Italy
[f] Centre for Neuroimaging Sciences, Institute of Psychology, Psychiatry and Neuroscience (IoPPN), King's College London, London, UK
[g] Department of Psychological Medicine, Institute of Psychiatry, Psychology and Neuroscience, King's College London, London, UK
[h] Psychosis Department, Institute of Psychiatry, Psychology and Neuroscience, King's College London, London, UK
[i] Department of Anesthesia, Critical Care and Pain Medicine, Massachusetts General Hospital, Harvard Medical School, Boston, MA, USA

ARTICLE INFO

Keywords:
Physics informed neural networks
PET
IDIF
AIF
Metabolic imaging
TSPO

ABSTRACT

Introduction: We propose a novel approach for the non-invasive quantification of dynamic PET imaging data, focusing on the arterial input function (AIF) without the need for invasive arterial cannulation.
Methods: Our method utilizes a combination of three-dimensional depth-wise separable convolutional layers and a physically informed deep neural network to incorporate*a priori* knowledge about the AIF's functional form and shape, enabling precise predictions of the concentrations of [^{11}C]PBR28 in whole blood and the free tracer in metabolite-corrected plasma.
Results: We found a robust linear correlation between our model's predicted AIF curves and those obtained through traditional, invasive measurements. We achieved an average cross-validated Pearson correlation of 0.86 for whole blood and 0.89 for parent plasma curves. Moreover, our method's ability to estimate the volumes of distribution across several key brain regions – without significant differences between the use of predicted versus actual AIFs in a two-tissue compartmental model – successfully captures the intrinsic variability related to sex, the binding affinity of the translocator protein (18 kDa), and age.
Conclusions: These results not only validate our method's accuracy and reliability but also establish a foundation for a streamlined, non-invasive approach to dynamic PET data quantification. By offering a precise and less invasive alternative to traditional quantification methods, our technique holds significant promise for expanding the applicability of PET imaging across a wider range of tracers, thereby enhancing its utility in both clinical research and diagnostic settings.

1. Introduction

Positron emission tomography (PET) is a nuclear medicine imaging technique that generates three-dimensional images of functional processes within the body [1]. A PET image is acquired following the injection of a labeled radiotracer, commonly e.g. [^{11}C] or [^{18}F], into the bloodstream. In clinical practice, PET data are typically acquired using a static acquisition protocol, resulting in a 3D image depicting the spatial distribution of the radiotracer at a single time-point in arbitrary or normalized units. In contrast, dynamic PET involves continuous data capture from the time of tracer injection hence providing information on tracer distribution over time [2–4]. Dynamic PET allows quantitative imaging via kinetic modeling, allowing the evaluation of parameters of interest, such as vascular transport, metabolic rate, and receptor density (depending on the specific tracer used) [5]. This analysis requires not only information about the tracer concentration in the tissue under investigation but also, critically, the estimation of the arterial input function (AIF), i.e., the concentration of the free tracer

* Corresponding author.
E-mail addresses: matteo.ferrante@uniroma2.it (M. Ferrante), marianna.inglese@uniroma2.it (M. Inglese).

https://doi.org/10.1016/j.cmpb.2024.108375
Received 21 March 2024; Received in revised form 14 July 2024; Accepted 14 August 2024
Available online 20 August 2024
0169-2607/© 2024 The Author(s). Published by Elsevier B.V. This is an open access article under the CC BY license (http://creativecommons.org/licenses/by/4.0/).

in the plasma over time, also called parent plasma curve, together with the quantification of the radiotracer concentration in the blood (called whole blood curve). Both whole blood and parent plasma curves are essential for characterizing the delivery and availability of the tracer to the tissue of interest, and are obtained through the invasive procedure of arterial cannulation [4] followed by numerous blood samples drawn during PET acquisitions. The invasive nature of AIF measurement presents challenges, including increased clinical staffing needs, patient discomfort, and the risk of adverse events, as well as the need for additional laboratory procedures. As a result, there is significant interest in developing non-invasive methods to estimate the AIF directly from dynamic PET images [3,6,7], potentially opening up the use of quantitative PET imaging to a much wider corpus of clinical centers.

Current image-derived input function (IDIF) approaches involve extracting tracer activity from arterial blood pools within the PET images. However, in brain PET studies, only small vessels, such as the carotid arteries, are available in the field of view, with a caliber of 4 to 5 mm, which is comparable to the spatial resolution of most clinical PET scanners (~5 mm) [6,8]. This introduces two related partial volume effect issues: the spill-out and spill-in effects, which not only impact the amplitude of the carotid signal but also its shape [3,6,8]. Importantly, IDIF estimation requires the quantification of radiometabolites in the plasma, which contribute to the total radioactivity measured in the blood [9]. Again, this latter correction necessitates for arterial cannulation and invasive blood samples for *in vitro* analysis [10].

This study introduces a physics-informed convolutional neural network designed to non-invasively generate both whole blood and, importantly, metabolite-corrected parent plasma curves from dynamic PET images. Since it is known that blood curves can consistently be described by a specific functional form resulting from the physical phenomena of fast uptake and slow washout, as outlined by the Parker model, this understanding has been embedded into the neural network to enhance its predictive accuracy. As validation, we employ [^{11}C]PBR28 PET images, i.e. a tracer where the estimation of the metabolite-corrected AIF is crucial for correct quantification. Our technique is then used for quantifying kinetic parameters associated with the expression of the translocator protein 18kDa (TSPO). TSPO, which is expressed in activated microglia, and also in astrocytes and endothelial cells, is known to be upregulated in neuro-immune responses, is generally assumed to be a biomarker for neuroinflammatory processes [11–15]. This makes TSPO the primary target for PET studies aimed at imaging neuroinflammation in vivo. The quantification of TSPO density with PET is challenging for multiple reasons. Firstly, there is a single nucleotide polymorphism in the TSPO gene which affects the binding affinity of second-generation TSPO PET tracers [16–19], generating the need for genetic screening in all patients in order to take this confound into account. Moreover, TSPO radioligands have affinity for plasma proteins whose concentration may vary in pathological conditions. While in principle measuring the plasma free fraction (FP) would account for this, in practice this measure is extremely challenging due to the very low FP values [20]. Recently, neural networks demonstrated promise in AIF estimation, integrating the differentiability of kinetic models and specific constraints into their network architecture and training process [6]. In our approach, we incorporate an *a priori* understanding of the AIF's functional form [21] into the network's architecture, proposing a physics-informed neural network (PINNs) suitable for robust learning from few noisy data. Additionally, we employ depthwise separable convolutional layers to efficiently learn spatiotemporal features from raw dynamic PET images. This methodology not only reduces the volume of data required by exploiting dynamic similarities across subjects, but also decreases the number of parameters necessary for training the model.

1.1. Related work

Recent advancements have led to the development of non-invasive methodologies for estimating AIF directly from imaging data [6,22,23] through either model-based or data-driven strategies. Model-based techniques [24] employ mathematical representations to simulate tracer kinetics within tissue and blood, thereby facilitating the AIF estimation from imaging data. Notable examples of this approach include Patlak graphical analysis [25], the bi-compartmental, and the tri-compartmental models. While effective, these methods necessitate predefined knowledge of tracer kinetics and tissue-specific physiological parameters, potentially limiting their broader applicability. Conversely, data-driven methodologies, such as those outlined in [26], leverage machine learning algorithms to estimate the AIF without the prerequisite of prior tracer kinetics or physiological parameter knowledge. However, these techniques often require extensive training data and may exhibit high sensitivity to the choice of training dataset.

In this study, we introduce a novel methodology that synergizes the strengths of both model-based and data-driven approaches. Our proposed method utilizes PINNs to estimate the AIF from PET imaging data. This technique innovatively combines deep learning algorithms with an embedded knowledge of the tracer dynamics in the blood. The network architecture is specifically designed to perform optimization within a solution space constrained by plausible values provided by a functional form which approximates the AIF with high accuracy [27], thereby enhancing the estimation and applicability of the AIF in dynamic PET imaging without arterial cannulation.

2. Material and methods

2.0.1. Patient population

The data used in this work were collected as part of several experimental medicine studies in neuroinflammation and made available by King's College London [28–30]. A total of 72 healthy volunteers (age (mean ± standard deviation) = 32 ± 13 years; sex: 50 male and 22 female) were included. Each participant underwent a 90 min [^{11}C]PBR28 PET, together with arterial blood sampling, and structural MRI acquisition in two separate visits. All studies were approved by local ethics committees and institutional review boards, and all participants provided written informed consent prior to enrollment. The inclusion criteria for study participants were aged above 18 years and capacity to give written informed consent. The exclusion criteria included any current or past significant medical condition, in particular any associated with inflammation, history and/or family history in first-degree relatives of any psychiatric disorder, as determined by the Structured Clinical Interview for DSM-IV Axis 1 Disorders, Clinician Version (SCID-CV), history of substance abuse/dependence or head injury; exposure to anti-inflammatory or benzodiazepine medications in the last month; significant prior exposure to radiation, pregnancy or breastfeeding. Full details on can be found in original Refs. [28–30]. All data were gathered from the KCL historical database. All studies were approved by local research ethics committees, including the Queen Square London Ethical committee, ref. 16/LO/1520, prior to study start, and all participants provided their informed consent to participate after reading a full description of the study.

2.0.2. Data acquisition

All PET scans were performed using a Siemens Biograph™ TruePoint™ PET CT scanner (Siemens Medical Systems, Germany), and included an initial low-dose CT scan, acquired for attenuation and scatter correction, followed by a continuous dynamic PET acquisition from 0 to 90 min after a bolus injection of [^{11}C]PBR28, with an injected dose of 330.60 ± 26.7 MBq (mean ± standard deviation). Radio-pharmaceutical preparation acquisition protocol was consistent for all the studies. Dynamic PET data were binned into 26 frames of duration 8 × 15 s, 3 × 1 min, 5 × 2 min, 5 × 5 min, 5 × 10 min. Data were reconstructed using filtered back projection with a 5 mm isotropic Gaussian smoothing, and corrected for random noise, attenuation, and scatter effects. Given the genetic rs6971 polymorphism of the TSPO gene, which determines a different affinity of the TSPO radioligands,

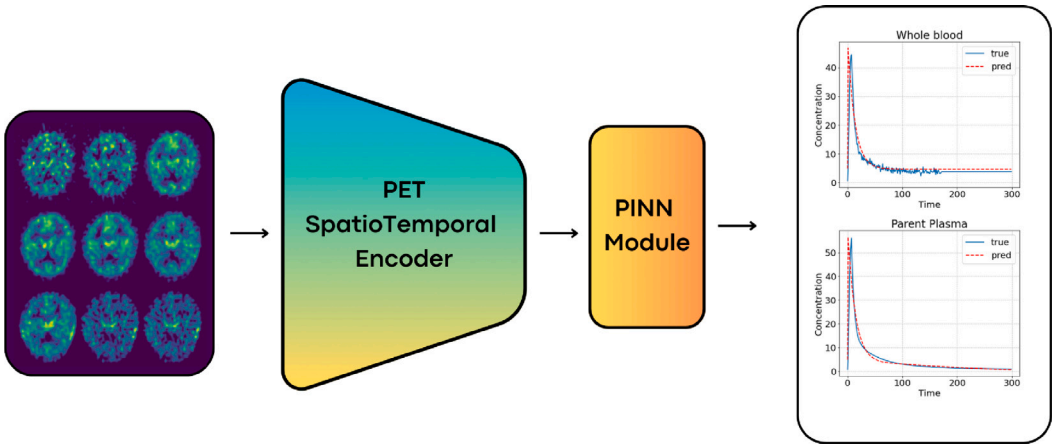

Fig. 1. Illustrative overview of our deep learning architecture for AIF estimation in dynamic PET imaging. This schematic delineates the data flow within the proposed architecture, beginning with input layers and progressing through various computational stages all the way to whole blood and parent plasma curves estimation. Each block in the diagram symbolizes a distinct computational unit or layer, designed to extract pertinent spatio-temporal features from the 4D PET datasets. These features are then integrated into the Physically-Informed Neural Network (PINN) module, which applies domain-specific constraints and curve shape considerations.

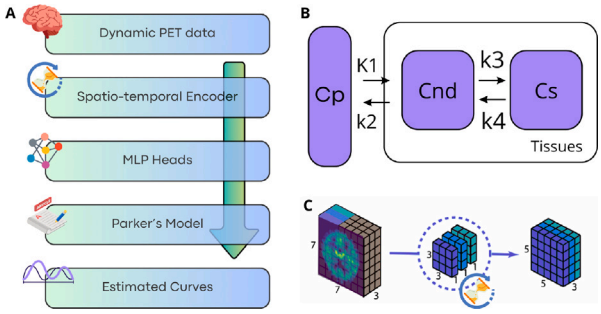

Fig. 2. Comprehensive diagrammatic representation of the proposed methodology and its constituent elements. (A) Depicts the systematic flow of information within the proposed methodology, illustrating the sequential steps and interactive processes integral to data processing and analysis. (B) Elucidates the compartmental model implemented for kinetic parameter estimation, delineating various compartments and elucidating their interdependencies. (C) Exhibits the implementation of the temporal depthwise convolution technique, a critical element of the methodology that facilitates effective and refined extraction of spatio-temporal features, thereby enhancing analytical precision.

all participants were genotyped before scanning and classified as high affinity binder (HAB), mixed affinity binder (MAB), or low affinity binder (LAB) [31]. Only HABs and MABs were retained for further analysis (50 HABs and 22 MABs). For all participants, arterial blood data were sampled during PET acquisition using the combination of an automatic continuous sampling system of the whole blood activity for the first 15 min of each scan and a series of discrete manual blood samples at 5, 10, 15, 20, 25, 30, 40, 50, 60, 70, 80, and 90 min. All manual samples were centrifuged and used to determine the plasma over blood activity ratio (POB); samples taken at 5, 10, 20, 30, 50, 70, and 90 min were also analyzed using radio-high performance liquid chromatography (HPLC) to calculate the fraction of parent tracer in arterial plasma, namely the parent plasma curve. Structural T1-weighted (T1w) MR images were acquired for each participant in separate visits using a Siemens 3-T MR scanner, using either a Siemens Tim Trio or Siemens MAGNETOM Verio model. Details on data acquisition are provided in original Refs. [28–30].

2.0.3. PET data pre-processing

All data were pre-processed with the same imaging pipeline using MIAKAT neuroimaging analysis toolbox (MIAKAT™, http://Invicro.org). The pipeline includes: (1) a step of motion correction of the dynamic PET data; (2) the computation of integral PET images; (3) the derivation of brain and grey matter masks from structural MR images and their registration to the subject's native PET space; (4) the coregistration of a neuroanatomical atlas (CIC atlas, version 2.046, included in MIAKAT) to the subject's PET native space and the definition of 125 regions of interest (ROIs); (5) the computation of mean regional Time Activity Curves (TACs), to minimize partial volume effects. TACs for representative ROIs, both cortical and subcortical (hippocampus, thalamus, caudate, putamen, parietal lobe, occipital and frontal lobes), were considered in this paper.

2.1. Physics-informed neural networks

Physics-Informed Neural Networks are a machine learning technique used to solve Partial Differential Equations (PDEs). They train a neural network to minimize a loss function, including initial and boundary conditions along the space–time domain's boundary and the PDE residual at selected points. They are unsupervised taking into account only the underlying PDE, i.e. the physics of the problem, rather than attempting to deduce the solution based solely on data, i.e. by fitting a neural network to a set of state-value pairs. This type of network proves particularly advantageous in scenarios with limited data availability and/or when strict adherence to known physical laws is critical, such as in fluid dynamics and material science [21]. Our method innovatively applies this concept to the quantification of dynamic [^{11}C]PBR28 PET data. It constrains the depthwise separable convolution-based spatiotemporal encoding within the confines of the Parker model (PM), which describes the AIF as a combination of two Gaussians and an exponential modulated by a sigmoid function [27]:

$$AIF(t) = \sum_{n=1}^{2} \frac{A_n}{\sigma_n\sqrt{2\pi}} e^{-\frac{(t-T_n)^2}{2\sigma_n^2}} + \alpha \frac{exp(-\beta t)}{1+exp(-s(t-\tau))} \quad (1)$$

Here, A_n, T_n, and σ_n are the scaling constants, centers, and widths of the nth Gaussian, respectively, while α and β represent the amplitude and decay constant of the exponential. The parameters s and τ define the width and center of the sigmoid, respectively.

Consequently, the extracted spatiotemporal features become pivotal in estimating the parameters of the PM. The incorporation of the PM into the PINN framework ensures that the predicted curves (both whole blood and parent plasma) adhere to the characteristic functional shape of the AIF. Notably, our proposed architecture is fully differentiable and therefore, during training, the mean squared error (MSE) loss is calculated between the actual and the network-predicted curves, facilitating end-to-end gradient back-propagation through both the deep learning components and the embedded physics-informed constraints.

To clarify, our Physics Informed Neural Network (PINN) framework can be mathematically framed as follows. Our input data consists of 4D pre-processed PET images, denoted as x, and we aim to predict an AIF curve, y. Our objective is to train a neural network $\hat{y} = f(x)$ such that $\|y - \hat{y}\|^2$ is minimized for all x. To achieve this goal, even in a low-data regime, our approach constrains the network to operate within the solution space defined by the family of functions described by the Parker model. Let us denote the Parker model as pm, which is a scalar function depending on certain parameters θ(i.e., $\theta = A_n, T_n, \sigma_n$) and time. Given this formulation, the problem now reduces to estimating θ. This simplifies our task to $f(x) = pm(g(x))$, where g is a neural network that estimates θ from the PET images, i.e., $\theta = g(x)$. With this problem decomposition, the neural network we are training is g, and we use a mean squared error loss to effectively minimize the error.

$$\mathcal{L} = \frac{1}{N}\sum_{i}^{N} |y - pm(g(x))|^2$$

2.2. Neural network architecture

The architecture (Fig. 1) comprises six depthwise separable 3D strided convolution layers, a key advancement in convolutional neural networks, efficiently reduce computational load and parameter count [32]. Differing from standard convolutional layers, which apply filters across all input channels, these layers perform the convolution in two stages. The first, depthwise convolution, uses distinct filters for each input channel (e.g., a 3 × 3 × 3 filter per depth slice in a 3D image). The second stage, pointwise convolution, combines these results, optionally increasing channel count. This architecture's main benefit is its reduced parameter count. For a 3D image with N input channels and M output channels, while traditional 3D convolutions with a 3 × 3 × 3 kernel require $N \times M \times K^3$ parameters, depthwise separable convolutions need just $N \times K^3$ for the depthwise stage and $N \times M$ for the pointwise stage.

In the specific domain of 4D dynamic PET imaging, which encompasses both spatial and temporal dimensions, conventional 4D convolutions can be prohibitively computationally intensive and susceptible to overfitting due to an excessive parameter count. By implementing 3D depthwise separable convolutions, temporal evolution within these images is encoded along the channel dimension. This approach facilitates the identification of spatial patterns within each temporal frame, followed by their integration across varying time points. For example, standard 4D convolutions initiating from N channels to M output channels demand NMK^4 parameters. In contrast, our proposed methodology necessitates merely $(NK^3 + NM)$ parameters. Illustratively, for an initial layer with 25 input channels (representing dynamic PET time points) and 128 output channels as a latent representation, and using a (3,3,3) kernel, a 4D convolution would require $25 \times 128 \times (3)^4 = 259200$ parameters. Our approach, aiming for an efficacious representation, employs only $25 \times 3^3 + 25 \times 128 = 3875$ parameters, thereby achieving a parameter reduction by nearly two orders of magnitude. This not only renders computation more feasible but also significantly diminishes the risk of overfitting due to overparametrization.

Following the convolution layers is an average pooling layer with a kernel size of 2. The extracted features are then flattened and fed into two separate heads that estimate the parameters of the PM for both the whole blood and parent plasma curves. Each head is a three-layer multilayer perceptron with hyperbolic tangent activation functions, mapping the features to the 10 parameters of the PM. The PM is integrated into the computational graph, enabling the generation of AIF estimates over 500 evenly sampled time points, which are compared to the original curves during training using MSE loss in a 5-fold cross-validation. This rotation of the validation set across folds ensures that each data point is predicted once, thereby enabling a thorough evaluation across the entire dataset. The model was trained on an NVIDIA A100 GPU (80 GB RAM; batch size: 20, 2500 epochs for each fold (5 folds, 420 min per fold), Adam optimizer, learning rate: 1e−4; reduced by 10% every 500 epochs). During inference, the network inputs the 4D pre-processed PET image, estimates the PM parameters, and employs them to predict the estimated curves.

2.3. Compartmental modeling framework

Post-training, the estimated curves from the neural network are employed to model [^{11}C]PBR28 kinetics using a two-tissue compartmental model (2TCM) (Fig. 2) [16]. The 2TCM, utilized outside the network, is defined by a set of differential equations describing the radiotracer exchange between different tissue compartments:

$$\frac{dC_{nd}(t)}{dt} = K_1 C_p(t) - (k_2 + k_3) C_{nd}(t) + k_4 C_s(t) \tag{2}$$

$$\frac{dC_s(t)}{dt} = k_3 C_{nd}(t) - k_4 C_s(t) \tag{3}$$

$$C_{nd}(0) = 0, \quad C_s(0) = 0 \tag{4}$$

$$C_{measured}(t) = (1 - V_b)[C_{nd}(t) + C_s(t)] + V_b C_b(t) \tag{5}$$

Here, $C_{measured}(t)$ is the dynamic PET signal, with $C_{nd}(t)$ and $C_s(t)$ representing the non-displaceable and specific tracer concentrations in tissue compartments, respectively. $C_b(t)$ and $C_p(t)$ denote tracer concentrations in whole blood and parent plasma (metabolite-corrected), estimated by our model. The rate constants k_1, k_2, k_3, and k_4 (expressed in units of mL/cm^3 per minute or 1/min) quantify tracer transport between plasma and tissue, and within tissue compartments. These constants allow the calculation of the volume of distribution v_T (mL/cm^3) as follows:

$$v_T = \frac{K_1}{k_2}\left(1 + \frac{k_3}{k_4}\right) \tag{6}$$

With the 2TCM, the volume of distribution is calculated fitting the cortical and subcortical TACs using the measured ("true") and predicted ("pred") whole blood and parent plasma curves. For a final comparison, it was also estimated using population averaged whole blood and plasma curves obtained from our cohort fitted with the PM ("parker").

2.4. Evaluation methodology

The validation of our model encompasses three critical aspects:

(1) **Accuracy Assessment of Predicted Curves**. The congruence between predicted and true curves is quantified using a number of statistical measures, including Mean Squared Error (MSE), Mean Absolute Error (MAE), Pearson Correlation Coefficient, the area under the plasma/blood curves (AIF_AUC) Difference, and R-Squared for a comprehensive view of the model's accuracy.

(2) **Replication of associations between kinetic modeling parameters and genetic or phenotypic traits**. Since a single nucleotide polymorphism in the TSPO gene impacts the binding affinity of the PET tracer affecting the measurement of its volume of distribution, we focused on examining variations in v_T associated with binding 'Affinity', i.e., in HAB and MAB. Also, since TSPO availability is also potentially conditioned by sex [33], we explored whether this effect could be observed using the measured curves and, if yes, observed using the predicted curves as well. In addition, in order to investigate the putative differences between quantitative PET parameters extracted from compartmental modeling (i.e., v_T, k_1, k_2, k_3, k_4 and v_B) using the measured, predicted and population averaged whole blood and parent plasma curves while also taking into account the effects of age, sex and genotype, we employed a linear mixed model. This model included both "between" effects (sex: 2 levels, i.e., M

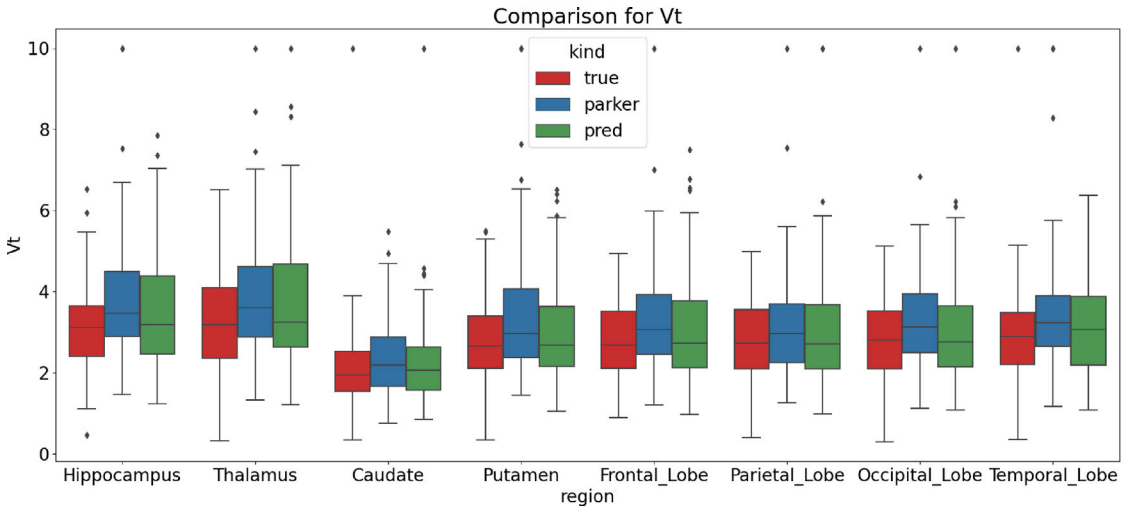

Fig. 3. Boxplots of v_T values obtained in sample ROIs when fitting the two-tissue compartmental model (2TCM) with both the measured ("true"), predicted ("pred") and population-averaged whole blood and parent plasma curves fitted with PM ("parker"). No statistical differences related to curve estimation methods were found.

and F; binding affinity: 2 levels, i.e., HAB and MAB; and age: continuous) and a "within" effect Curve_Type: 3 levels, i.e., true, predicted, and population-averaged. Additional model terms are explained in the next section.

(3) **Interaction Effects** The linear mixed model also incorporated interactions of all "between" effects with the "within" effect (i.e. curve type). This is an important target since the interactions test whether the estimation method influenced the relationships between the quantitative PET biomarkers extracted from the 2TCM and biological variables (sex, binding affinity, and age). The analysis was conducted using Restricted Maximum Likelihood (REML) estimation, with criteria including the Satterthwaite method for degrees of freedom and a 95% confidence interval.

3. Results

The evaluation of our model's performance in estimating whole blood and parent plasma curves, in comparison to the measured ones, is presented in Table 2 (see Fig. 4).

Fig. 5 shows a comparison between the v_T obtained fitting the 2TCM using the actual (true) and predicted (pred) whole blood and parent plasma curves. Specifically, the scatterplot indicates a R^2 of 0.65 between true and predicted v_T. The Bland-Altman plot shows the average difference between true and predicted v_T centered close to 0 and grouped (with the exception of 5 values) in the 95th percentile. The boxplots in Fig. 3 show the v_T of [^{11}C]PBR28 in the hippocampus, thalamus, caudate, putamen, parietal, occipital and frontal lobes.

Further, the v_T obtained by fitting the 2TCM using population-averaged whole blood and parent plasma curves as modeled by the PM (Parker) did not demonstrate a statistically significant main effect of the curve type. This supports our result: the quantitative outcome of PET parameter estimation is not affected by the type of input curve, whether it is the measured one, the predicted one, or the population-averaged one. Crucially, we have demonstrated that these results can now be achieved without the need for invasive measurements of the radiotracer concentration in the blood. This advancement is significant as it validates the feasibility of using different curve types interchangeably in compartmental modeling. This finding is significant, as it suggests the feasibility of using different curve types interchangeably in compartmental modeling without compromising the integrity and accuracy of the results. This flexibility in curve choice can be particularly beneficial in scenarios where actual curve data is challenging to obtain, allowing

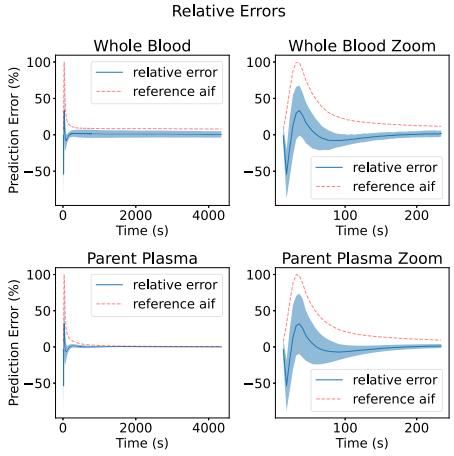

Fig. 4. Quantitative assessment of prediction accuracy: The left panels represent the relative error between measured and predicted curves across the full time scale, while the right panels provide a detailed view of the critical peak and fall-off regions. The solid line indicates the mean relative (percentage) error, and the shaded areas correspond to the standard deviations, illustrating the precision of the predictions over time. To guide the interpretation, the dotted red line is the average whole blood and parent plasma curve. That helps to visually match errors with peak, decay and tail, normalized to have the maximum at one for ease of visualization.

for alternative methods to be employed without a significant loss in data quality or reliability. The influence of binding affinity, is pivotal in the context of radiotracer uptake, reflecting a nuanced interplay between the tracer's characteristics and the biological makeup of the subject, while the impact of sex on v_T has been observed, albeit inconsistently. In this respect, our analysis consistently revealed a significant effect of binding affinity and sex on the quantitative PET parameters, but no interaction with the factor which encodes the type of curve. The first finding aligns with existing literature, underscoring the critical role these biological factors play in influencing PET imaging outcomes. Importantly, the second finding indicates that these effects are correctly reproduced using our estimated curves. Similarly, we reproduced the impact of sex on these parameters which we observed on our data using the true curves, but found no interaction of the sex factor with the curve type factor, indicating again that these effects are correctly reproduced using our estimated curves. A graphical representation of these results can be found in Fig. 6

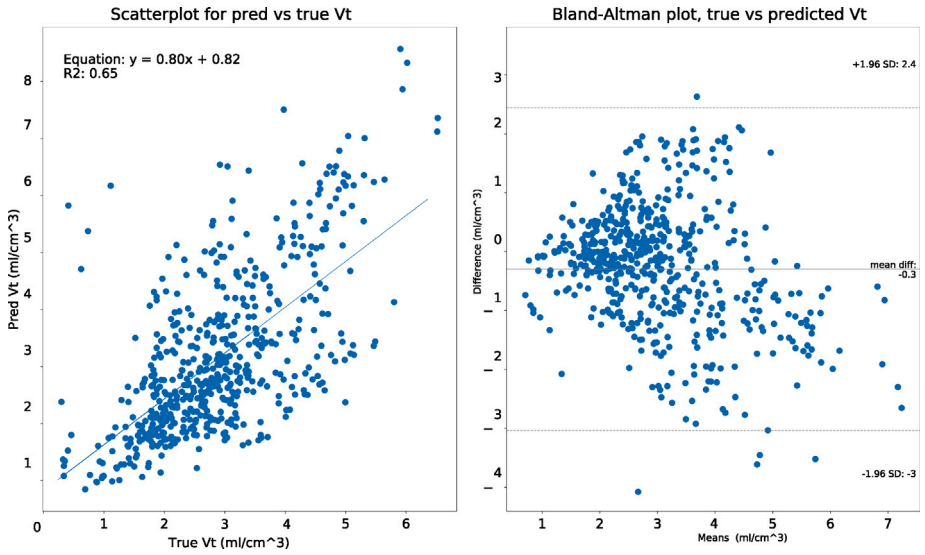

Fig. 5. Left: Scatterplot between predicted and true v_T values. Right: Bland Altman plot of the same data.

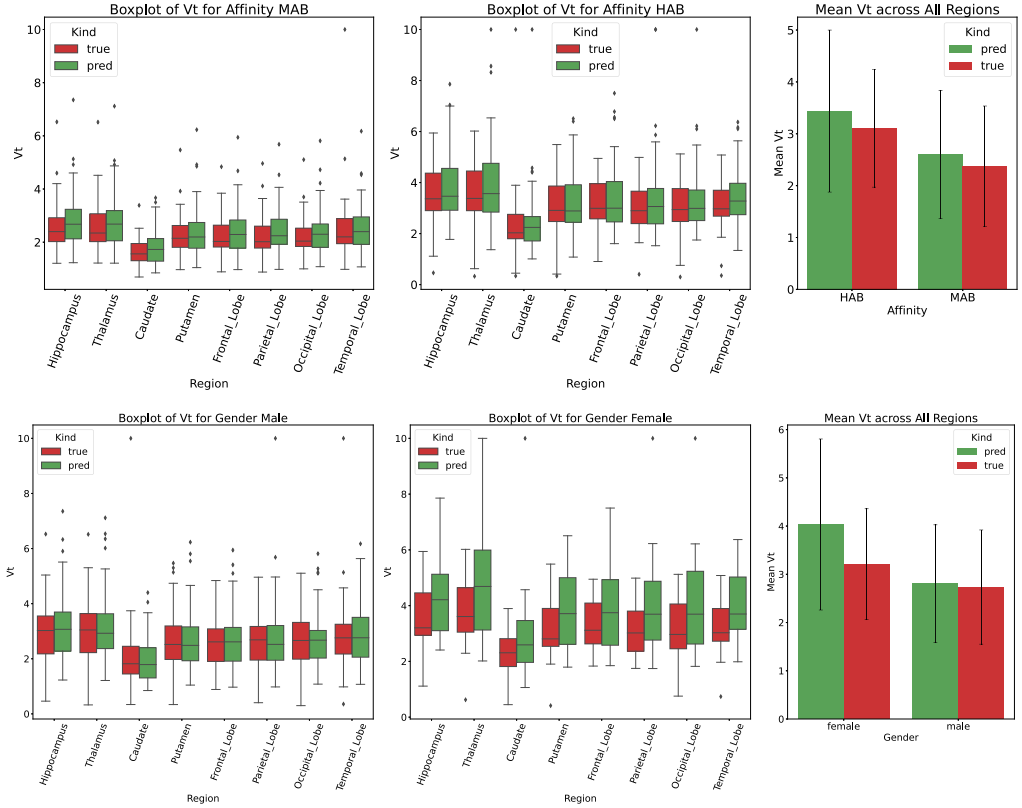

Fig. 6. Sex Effect on v_T evidenced using v_T computed from measured ("true") and predicted ("pred") curves. No statistical differences related to the curve reconstruction method were found.

In the supplementary materials, we show the result of the full compartmental analysis with the calculation of the rate constants K_1, k_2, k_3, k_4 and v_b, using the 2TCM fitted to the predicted curves and, for comparative analysis, to the measured and, finally, to the population-averaged whole blood and parent plasma curves fitted with the PM. Supplementary Tables present the outcomes of the linear mixed model on those parameters. Generally, the rate constants derived from our predicted curves did not show statistically significant differences compared to those obtained from the measured and population-averaged curves (Parker) ($p > 0.05$), and interaction effects (see above) where seldom observed.

4. Discussion

Compartmental modeling in dynamic PET imaging offers significant advantages over the Standardized Uptake Value (SUV) method by providing a more detailed and accurate quantitative analysis of tracer kinetics. Unlike the semi-quantitative SUV, which can be influenced by external factors and provides only a static snapshot of tracer uptake, compartmental modeling accounts for the dynamic movement of tracers across physiological compartments, offering enhanced accuracy and specificity. This approach yields deeper insights into physiological and pathological processes, aiding in disease characterization and treatment

Table 1
Region-wise result of statistical analysis of v_T values using a mixed model which includes interactions. We analyze the effects on v_T obtained by fitting the two-tissue compartmental model with the measured, population-averaged fitted with the PM, and predicted whole blood and parent plasma curves, as well as the effects of sex, binding affinity, age, and relative interactions.

Region	Source	Statistic (F)	p-value
Frontal lobe	Sex	39.110771	0.0*
	Affinity	32.15778	0.0*
	Curve_Type	0.047779	0.953361
	Age	6.161004	0.013913*
	Sex * Curve_Type	1.850778	0.161259
	Affinity * Curve_Type	0.048326	0.952841
	Curve_Type * age	0.55812	0.573659
Hippocampus	Sex	19.473315	0.000017*
	Affinity	21.330053	0.000007*
	Curve_Type	1.000768	0.370253
	Age	6.637887	0.010718*
	Sex * Curve_Type	1.029932	0.359763
	Affinity * Curve_Type	0.0732	0.929451
	Curve_Type * age	3.259171	0.041402*
Occipital lobe	Sex	24.735298	0.000001*
	Affinity	15.941296	0.000093*
	Curve_Type	0.471981	0.624793
	Age	1.807532	0.18038
	Sex * Curve_Type	1.937423	0.148068
	Affinity * Curve_Type	0.873729	0.419744
	Curve_Type * age	0.488652	0.614536
Parietal lobe	Sex	29.152722	0.0*
	Affinity	23.510766	0.000003*
	Curve_Type	0.124759	0.882826
	Age	5.762825	0.017406*
	Sex * Curve_Type	2.413949	0.093884
	Affinity * Curve_Type	0.100272	0.904669
	Curve_Type * age	1.64521	0.197383
Putamen	Sex	25.560794	0.000001*
	Affinity	16.596922	0.000069*
	Curve_Type	0.844635	0.431718
	Age	17.265875	0.00005*
	Sex * Curve_Type	2.528895	0.083094
	Affinity * Curve_Type	0.000458	0.999542
	Curve_Type * age	3.522516	0.031955*
Temporal lobe	Sex	26.950623	0.000001*
	Affinity	16.620629	0.000066*
	Curve_Type	0.009846	0.990203
	Age	6.757094	0.01003*
	Sex * Curve_Type	3.248023	0.041712*
	Affinity * Curve_Type	0.864578	0.423401
	Curve_Type * age	0.824277	0.440608
Thalamus	Sex	28.710838	0.0*
	Affinity	25.16891	0.000001*
	Curve_Type	1.350943	0.262756
	Age	1.620444	0.204552
	Sex * Curve_Type	1.587303	0.208575
	Affinity * Curve_Type	0.213824	0.807786
	Curve_Type * age	2.993246	0.053735

* A statistical significant difference (p-value < 0.05).

Table 2
Comparative evaluation of model performance metrics for whole blood and parent plasma curve predictions. Each metric is presented as a mean value with its corresponding standard deviation, encapsulating the model's accuracy and consistency. This table highlights the AUC_AIF, correlation, and overall fit, offering a comprehensive view of the model's performance in predicting both whole blood and parent plasma curves, as compared to the measured ones.

Metric	Whole blood (Mean ± Std)	Parent plasma (Mean ± Std)
AIF_AUC difference	275.35 ± 832.07	93.66 ± 248.59
AIF_AUC % difference	−1.9 ± 28	−2.8 ± 14
Time to peak Diff %	0.4 ±1	0.4 ±1
MAE	2.15 ± 0.86	1.17 ± 0.30
MSE	18.35 ± 10.31	20.25 ± 7.58
Pearson Correlation	0.86 ± 0.02	0.89 ± 0.01
R^2	0.74 ± 0.03	0.80 ± 0.03

planning. Its ability to factor in individual variations makes it particularly valuable in personalized medicine, offering a more comprehensive understanding of complex biological functions than the simpler SUV measurement. The arterial input function – the temporal concentration profile of parent tracer in plasma – is essential for quantifying dynamic PET data to extract kinetic parameters. These parameters describe the radiotracer interaction within the target tissue (e.g., vascular transport and cellular metabolism) and are often used, together semi-quantitative parameters (e.g., SUV), for therapeutic response monitoring, prognosis evaluation, and cancer diagnosis or staging [34–38]. Conventionally, AIF measurement requires arterial cannulation during dynamic PET acquisition, a process that limits the technique's use in clinical research due to its invasiveness [4]. Existing non invasive alternative still present major limitations: population averaged approaches generally suffer from misestimation of the peak and metabolite fraction; IDIF approaches on the other hand suffer fron PV effects and the need for in vitro analysis of blood samples for, in case of specific tracers like [^{11}C]PBR28, the correction for the presence of radiometabolites in the plasma [3,9,39]. In fact, PET radiotracers undergo various biotransformations, resulting in different chemical entities and a decrease in the parent radiotracer's concentration. The PET scanner measures total radioactivity in tissue but cannot distinguish the chemical nature of the accumulated radiotracers. Quantifying the fraction of the parent radiotracer in tissue, derived from its plasma concentration, is crucial for fitting pharmacokinetic models and determining rate constants [40]. Our model addresses this challenge by predicting both the concentration of the parent tracer in plasma and whole blood, incorporating prior knowledge about the AIF's functional form. A significant innovation in this study is employing PINNs to predict blood and plasma curves, enhancing prediction accuracy by considering the input function's functional form. Our results, particularly the Pearson Correlation and R^2 values presented in Table 2, demonstrate the model's ability to accurately replicate the dynamics of whole blood and parent plasma curves. Specifically, an average cross-validated Pearson correlation (measured vs. predicted) of 0.86 and 0.89 for whole blood and parent plasma curves, respectively, was found demonstrating the model's effectiveness in capturing the tracer dynamics in the blood, including metabolic effects.

Another challenge was managing the small dataset of high-dimensional data (4D dynamic PET data). We addressed this by encoding time evolution in the channel dimension of 3D convolutional filters and using depthwise separable convolutions. This approach efficiently captures relevant dynamics from PET time series in a parameter-efficient manner. Additionally, we relied on a preprocessing pipeline that improved image quality to enhance the accuracy and reliability of the PET analysis, ensuring meaningful and precise quantification results. The impact of motion correction [41], the registration to the MNI space [42] and the computation of average regional TACs [43] on the quantification of kinetic parameters has been widely demonstrated.

The robustness of our method is further evidenced by pharmacokinetic assessments showing, notwithstanding a percentage difference between the time to the predicted and true blood/plasma curves' peaks of 0.4 ± 1% indicating a very good match between predicted and real time of peak occurrence and no statistical difference in the volumes of distribution obtained with the 2TCM using both true and predicted blood and plasma curves. In some cases, the model underestimated the distribution volume (v_T), as shown in Fig. 5. Given the known impact of arterial input function (AIF) peak heights on the quantification of dynamic PET data [44], we investigated the relationship between the shapes of the whole blood and plasma curves and the estimated v_T in a simulation study. In this study, the peaks of the parent plasma and whole blood curves were varied 100 times, ranging from −20% to 100% of their initial values. The scatterplots in Supplementary Figure V reveal

a strong negative correlation between the variation in (calculated as the difference between the predicted and true v_T for a representative patient) and the variation in the peaks of the parent plasma and whole blood curves (R^2 = 0.94 and R^2 = 0.93, respectively). This suggests that the underestimation of the distribution volume seen in Fig. 5 likely occurred when the model overestimated the AIF peaks, which happened in 25% of cases. This was further confirmed by the negative trend of the linear fits in Supplementary Figure V, where the difference between predicted and true v_T values for our cohort was plotted against the variation in the parent plasma and whole blood peaks (comparing the true values to those estimated by the model). Future work could address this issue by incorporating additional terms in the loss function to account for these factors more explicitly.

The effect of using measured/population-averaged and whole-blood and parent plasma curves fitted with the PM on Vt estimation, as well as on sex, binding affinity, and age, was analyzed with a linear mixed-effects model, and the results are summarized in Table 1. The binding affinity consistently shows high statistical significance across all regions, as well as interactions between factors such as sex, the type of curve, and age. This result indicates the complexity of these relationships and their impact on the quantification of PET data. Despite this, no significant differences in the outcomes of kinetic modeling were observed when comparing measured data with our model's estimations. Volumes of distribution obtained with our predicted blood and plasma curves are affected by TSPO binding affinity and sex in the same way as the real ones, demonstrating the same sensitivity to the inner variability of our cohort. Of note, the model was able to capture the single-subject variability of our PET scans, outperforming the measurements obtained using the population-averaged blood and plasma curves. Furthermore, the volumes of distribution obtained using our predicted curves successfully reproduced its inner variability given by the sex and the presence, in our cohort, of high and mild TSPO affinity binders [16–18], as compared to quantification using the measured curves. This outcome holds promise for broader acceptance within the nuclear medicine community, particularly for studies involving TSPO density in neuroinflammation [45].

Our study has limitations. The dataset's modest size raises concerns about potential systematic biases and makes it difficult to generalize the patients of other sites, especially in estimating critical parameters like the AIF peak/tail. Furthermore, the model has not been tested on healthy controls or in a cohort where blood tracer distribution and radiometabolites concentration is altered by clinical conditions or PET studies with pharmacological challenges. This latter research would be part of a separate study focused on the generalizability of our technique to situations where tracer metabolism and kinetics are altered by physiopathology. Finally, it is worth noting that, since this study was conducted on pre-existing data, the time resolution was not optimized for the specific objective of defining an image-derived input function. Instead, this framing has been optimized for brain kinetic modeling over the years and with hundreds of scans.

5. Conclusions

This study demonstrates the significant potential of integrating prior knowledge into neural networks for the modeling of complex biomedical phenomena, particularly the arterial input function, in the context of limited data availability. Our methodology, which employs depthwise separable convolutions along with physics-informed constraints, has shown notable effectiveness in the accurate approximation of the concentration of [^{11}C]PBR28 in the whole blood as well as in the parent plasma, indirectly demonstrating that information about tracer metabolism can be retrieved from PET imaging alone. Of note, our model was able to capture, solely from the image, the distribution of the tracer in the various blood compartments, which include the plasma and total blood but, more importantly, the radiometabolites partition.

The results of this study are promising, as they indicate no significant differences in the outcomes of kinetic modeling when comparing measured data with our model's estimations. Volumes of distribution obtained with our predicted blood and plasma curves are affected by TSPO binding affinity and sex, in the same way as the real ones are, demonstrating the same sensitivity to the inner variability of our cohort.

Our findings mark a significant step forward in the development of more patient-friendly and non-invasive PET techniques. By reducing the reliance on invasive procedures for quantitative analysis, this study contributes to the broader goal of making quantitative PET a more accessible and standard tool in clinical diagnostics. Such advancements hold the promise of transforming PET imaging into a more universally applicable and patient-centric diagnostic modality in healthcare.

CRediT authorship contribution statement

Matteo Ferrante: Writing – review & editing, Writing – original draft, Visualization, Validation, Software, Resources, Methodology, Investigation, Formal analysis, Conceptualization. **Marianna Inglese:** Writing – review & editing, Writing – original draft, Validation, Methodology, Formal analysis, Conceptualization. **Ludovica Brusaferri:** Writing – review & editing, Validation, Data curation. **Alexander C. Whitehead:** Writing – review & editing. **Lucia Maccioni:** Writing – review & editing, Data curation. **Federico E. Turkheimer:** Data curation. **Maria A. Nettis:** Data curation. **Valeria Mondelli:** Data curation. **Oliver Howes:** Data curation. **Marco L. Loggia:** Writing – review & editing, Validation, Supervision, Formal analysis. **Mattia Veronese:** Writing – review & editing, Validation, Data curation, Conceptualization. **Nicola Toschi:** Writing – review & editing, Supervision, Funding acquisition.

Declaration of competing interest

The authors declare that they have no known competing financial interests or personal relationships that could have appeared to influence the work reported in this paper.

Acknowledgments

This work is supported and funded by: NEXTGENERATIONEU (NGEU); the Ministry of University and Research (MUR); the National Recovery and Resilience Plan (NRRP); project MNESYS (PE0000006, to NT) - A Multiscale integrated approach to the study of the nervous system in health and disease (DN. 1553 11.10.2022); the MUR-PNRR M4C2I1.3 PE6 project PE00000019 Heal Italia (to NT); the NATIONAL CENTRE FOR HPC, BIG DATA AND QUANTUM COMPUTING, within the spoke "Multiscale Modeling and Engineering Applications" (to NT); the European Innovation Council (Project CROSSBRAIN - Grant Agreement 101070908, Project BRAINSTORM - Grant Agreement 101099355); the Horizon 2020 research and innovation Programme (Project EXPERIENCE - Grant Agreement 101017727). Matteo Ferrante is a Ph.D. student enrolled in the National PhD in Artificial Intelligence, XXXVII cycle, course on Health and Life Sciences, organized by Università Campus Bio-Medico di Roma.

Appendix A. Supplementary data

Supplementary material related to this article can be found online at https://doi.org/10.1016/j.cmpb.2024.108375.

References

[1] D.L. Bailey, D.W. Townsend, P.E. Valk, M.N. Maisey, Positron Emission Tomography: Basic Sciences, Springer London, 2005.
[2] K.C. Schmidt, F.E. Turkheimer, Kinetic modeling in positron emission tomography, Q. J. Nucl. Med. 46 (1) (2002) 70–85.

[3] Lioe-Fee de Geus-Oei, Eric P Visser, Paul FM Krabbe, Bas A van Hoorn, Emile B Koenders, Antoon T Willemsen, Jan Pruim, Frans HM Corstens, Wim JG Oyen, Comparison of image-derived and arterial input functions for estimating the rate of glucose metabolism in therapy-monitoring 18F-FDG PET studies, J. Nucl. Med. 47 (6) (2006) 945–949.

[4] Mark Muzi, Finbarr O'Sullivan, David A Mankoff, Robert K Doot, Larry A Pierce, Brenda F Kurland, Hannah M Linden, Paul E Kinahan, Quantitative assessment of dynamic PET imaging data in cancer imaging, Magn. Reson. Imaging 30 (9) (2012) 1203–1215.

[5] Ronald Boellaard, Standards for PET image acquisition and quantitative data analysis, J. Nucl. Med. 50 Suppl 1 (Suppl 1) (2009) 11S–20S.

[6] Paolo Zanotti-Fregonara, Kewei Chen, Jeih-San Liow, Masahiro Fujita, Robert B Innis, Image-derived input function for brain PET studies: many challenges and few opportunities, J. Cereb. Blood Flow Metab. 31 (10) (2011) 1986–1998.

[7] Matteo Ferrante, Marianna Inglese, Ludovica Brusaferri, Alexander Whitehead, Marco Loggia, Nicola Toschi, Physically informed neural network for non-invasive arterial input function estimation in dynamic PET imaging, in: Medical Imaging with Deep Learning, 2022.

[8] Tommaso Volpi, Lucia Maccioni, Maria Colpo, Giulia Debiasi, Amedeo Capotosti, Tommaso Ciceri, Richard E Carson, Christine DeLorenzo, Andreas Hahn, Gitte Moos Knudsen, Adriaan A Lammertsma, Julie C Price, Vesna Sossi, Guobao Wang, Paolo Zanotti-Fregonara, Alessandra Bertoldo, Mattia Veronese, An update on the use of image-derived input functions for human PET studies: new hopes or old illusions? EJNMMI Res. 13 (1) (2023) 97.

[9] Matteo Tonietto, Gaia Rizzo, Mattia Veronese, Masahiro Fujita, Sami S Zoghbi, Paolo Zanotti-Fregonara, Alessandra Bertoldo, Plasma radiometabolite correction in dynamic PET studies: Insights on the available modeling approaches, J. Cereb. Blood Flow Metab. 36 (2) (2016) 326–339.

[10] Richard Aarnio, Obada M Alzghool, Saara Wahlroos, James O'Brien-Brown, Michael Kassiou, Olof Solin, Juha O Rinne, Sarita Forsback, Merja Haaparanta-Solin, Novel plasma protein binding analysis method for a PET tracer and its radiometabolites: A case study with [11C]SMW139 to explain the high uptake of radiometabolites in mouse brain, J. Pharm. Biomed. Anal. 219 (114860) (2022) 114860.

[11] Marco L Loggia, Daniel B Chonde, Oluwaseun Akeju, Grae Arabasz, Ciprian Catana, Robert R Edwards, Elena Hill, Shirley Hsu, David Izquierdo-Garcia, Ru-Rong Ji, Misha Riley, Ajay D Wasan, Nicole R Zürcher, Daniel S Albrecht, Mark G Vangel, Bruce R Rosen, Vitaly Napadow, Jacob M Hooker, Evidence for brain glial activation in chronic pain patients, Brain 138 (Pt 3) (2015) 604–615.

[12] Jonas Hannestad, Jean-Dominique Gallezot, Thomas Schafbauer, Keunpoong Lim, Tracy Kloczynski, Evan D Morris, Richard E Carson, Yu-Shin Ding, Kelly P Cosgrove, Endotoxin-induced systemic inflammation activates microglia: [^{11}C]PBR28 positron emission tomography in nonhuman primates, Neuroimage 63 (1) (2012) 232–239.

[13] Nicole R Zürcher, Marco L Loggia, Robert Lawson, Daniel B Chonde, David Izquierdo-Garcia, Julia E Yasek, Oluwaseun Akeju, Ciprian Catana, Bruce R Rosen, Merit E Cudkowicz, Jacob M Hooker, Nazem Atassi, Increased in vivo glial activation in patients with amyotrophic lateral sclerosis: assessed with [(11)C]-PBR28, NeuroImage Clin. 7 (2015) 409–414.

[14] Erik Nutma, Jodie A Stephenson, Rianne P Gorter, Joy de Bruin, Deirdre M Boucherie, Cornelius K Donat, Marjolein Breur, Paul van der Valk, Paul M Matthews, David R Owen, Sandra Amor, A quantitative neuropathological assessment of translocator protein expression in multiple sclerosis, Brain 142 (11) (2019) 3440–3455.

[15] Jasmina Dimitrova-Shumkovska, Ljupcho Krstanoski, Leo Veenman, Diagnostic and therapeutic potential of TSPO studies regarding neurodegenerative diseases, psychiatric disorders, alcohol use disorders, traumatic brain injury, and stroke: An update, Cells 9 (4) (2020) 870.

[16] Gaia Rizzo, Mattia Veronese, Matteo Tonietto, Benedetta Bodini, Bruno Stankoff, Catriona Wimberley, Sonia Lavisse, Michel Bottlaender, Peter S Bloomfield, Oliver Howes, Paolo Zanotti-Fregonara, Federico E Turkheimer, Alessandra Bertoldo, Generalization of endothelial modelling of TSPO PET imaging: Considerations on tracer affinities, J. Cereb. Blood Flow Metab. 39 (5) (2019) 874–885.

[17] Neydher Berroterán-Infante, Monika Tadić, Marcus Hacker, Wolfgang Wadsak, Markus Mitterhauser, Binding affinity of some endogenous and synthetic TSPO ligands regarding the rs6971 polymorphism, Int. J. Mol. Sci. 20 (3) (2019).

[18] Franziska J Vettermann, Stefanie Harris, Julia Schmitt, Marcus Unterrainer, Simon Lindner, Boris-Stephan Rauchmann, Carla Palleis, Endy Weidinger, Leonie Beyer, Florian Eckenweber, Sebastian Schuster, Gloria Biechele, Christian Ferschmann, Vladimir M Milenkovic, Christian H Wetzel, Rainer Rupprecht, Daniel Janowitz, Katharina Buerger, Robert Perneczky, Günter U Höglinger, Johannes Levin, Christian Haass, Joerg C Tonn, Maximilian Niyazi, Peter Bartenstein, Nathalie L Albert, Matthias Brendel, Impact of TSPO receptor polymorphism on [18F]GE-180 binding in healthy brain and pseudo-reference regions of neurooncological and neurodegenerative disorders, Life (Basel) 11 (6) (2021) 484.

[19] David R Owen, Astrid J Yeo, Roger N Gunn, Kijoung Song, Graham Wadsworth, Andrew Lewis, Chris Rhodes, David J Pulford, Idriss Bennacef, Christine A Parker, Pamela L StJean, Lon R Cardon, Vincent E Mooser, Paul M Matthews, Eugenii A Rabiner, Justin P Rubio, An 18-kDa translocator protein (TSPO) polymorphism explains differences in binding affinity of the PET radioligand PBR28, J. Cereb. Blood Flow Metab. 32 (1) (2012) 1–5.

[20] Federico E Turkheimer, Gaia Rizzo, Peter S Bloomfield, Oliver Howes, Paolo Zanotti-Fregonara, Alessandra Bertoldo, Mattia Veronese, The methodology of TSPO imaging with positron emission tomography, Biochem. Soc. Trans. 43 (4) (2015) 586–592.

[21] M. Raissi, P. Perdikaris, G.E. Karniadakis, Physics-informed neural networks: A deep learning framework for solving forward and inverse problems involving nonlinear partial differential equations, J. Comput. Phys. 378 (2019) 686–707.

[22] Antonia Dimitrakopoulou-Strauss, Leyun Pan, Christos Sachpekidis, Kinetic modeling and parametric imaging with dynamic PET for oncological applications: general considerations, current clinical applications, and future perspectives, Eur. J. Nucl. Med. Mol. Imaging 48 (1) (2021) 21–39.

[23] Chul Hyoung Lyoo, Paolo Zanotti-Fregonara, Sami S. Zoghbi, Jeih-San Liow, Rong Xu, Victor W. Pike, Carlos A. Zarate Jr., Masahiro Fujita, Robert B. Innis, Image-derived input function derived from a supervised clustering algorithm: Methodology and validation in a clinical protocol using [11C](R)-rolipram, PLOS ONE 9 (2) (2014) 1–8.

[24] Hamed Moradi, Viktor Vegh, David Reutens, Non-invasive input function extraction from dynamic PET using machine learning along with an iterative approach, J. Nucl. Med. 62 (supplement 1) (2021) 1416.

[25] C.S. Patlak, R.G. Blasberg, J.D. Fenstermacher, Graphical evaluation of blood-to-brain transfer constants from multiple-time uptake data, J. Cereb. Blood Flow Metab. 3 (1) (1983) 1–7.

[26] Francesca Zanderigo, Ramin V. Parsey, R. Todd Ogden, Model-free quantification of dynamic PET data using nonparametric deconvolution, J. Cereb. Blood Flow Metab. 35 (8) (2015) 1368–1379.

[27] Geoff J M Parker, Caleb Roberts, Andrew Macdonald, Giovanni A Buonaccorsi, Sue Cheung, David L Buckley, Alan Jackson, Yvonne Watson, Karen Davies, Gordon C Jayson, Experimentally-derived functional form for a population-averaged high-temporal-resolution arterial input function for dynamic contrast-enhanced MRI, Magn. Reson. Med. 56 (5) (2006) 993–1000.

[28] Peter S Bloomfield, Sudhakar Selvaraj, Mattia Veronese, Gaia Rizzo, Alessandra Bertoldo, David R Owen, Michael Ap Bloomfield, Ilaria Bonoldi, Nicola Kalk, Federico Turkheimer, Philip McGuire, Vincenzo de Paola, Oliver D Howes, Microglial activity in people at ultra high risk of psychosis and in schizophrenia: An [(11)C]PBR28 PET brain imaging study, Am. J. Psychiatry 173 (1) (2016) 44–52.

[29] Tarik Dahoun, Marilia A Calcia, Mattia Veronese, Peter Bloomfield, Tiago Reis Marques, Federico Turkheimer, Oliver D Howes, The association of psychosocial risk factors for mental health with a brain marker altered by inflammation: A translocator protein (TSPO) PET imaging study, Brain Behav. Immun. 80 (2019) 742–750.

[30] M A Nettis, M Veronese, N Nikkheslat, N Mariani, G Lombardo, L Sforzini, D Enache, N A Harrison, F E Turkheimer, V Mondelli, C M Pariante, PET imaging shows no changes in TSPO brain density after IFN-α immune challenge in healthy human volunteers, Transl. Psychiatry 10 (1) (2020) 89.

[31] Catriona Wimberley, Sonia Lavisse, Ansel Hillmer, Rainer Hinz, Federico Turkheimer, Paolo Zanotti-Fregonara, Kinetic modeling and parameter estimation of TSPO PET imaging in the human brain, Eur. J. Nucl. Med. Mol. Imaging 49 (1) (2021) 246–256.

[32] François Chollet, Xception: Deep learning with depthwise separable convolutions, 2017.

[33] Jouni Tuisku, Pontus Plavén-Sigray, Edward C Gaiser, Laura Airas, Haidar Al-Abdulrasul, Anna Brück, Richard E Carson, Ming-Kai Chen, Kelly P Cosgrove, Laura Ekblad, Irina Esterlis, Lars Farde, Anton Forsberg, Christer Halldin, Semi Helin, Eva Kosek, Mats Lekander, Noora Lindgren, Päivi Marjamäki, Eero Rissanen, Marcus Sucksdorff, Andrea Varrone, HRRT [11C]PBR28 study group, Karin Collste, Jean-Dominique Gallezot, Ansel Hillmer, Yiyun Huang, Caroline O Höglund, Jarkko Johansson, Aurelija Jucaite, Jon Lampa, Nabeel Nabulsi, Brian Pittman, Christine M Sandiego, Per Stenkrona, Juha Rinne, David Matuskey, Simon Cervenka, Effects of age, BMI and sex on the glial cell marker TSPO - a multicentre [11C]PBR28 HRRT PET study, Eur. J. Nucl. Med. Mol. Imaging 46 (11) (2019) 2329–2338.

[34] Antonia Dimitrakopoulou-Strauss, Leyun Pan, Christos Sachpekidis, Parametric imaging with dynamic PET for oncological applications: Protocols, interpretation, current applications and limitations for clinical use, Semin. Nucl. Med. 52 (3) (2022) 312–329.

[35] Rohini Sharma, Pablo Oriol Valls, Marianna Inglese, Suraiya Dubash, Michelle Chen, Hani Gabra, Ana Montes, Amarnath Challapalli, Mubarik Arshad, George Tharakan, Ed Chambers, Tom Cole, Jingky P Lozano-Kuehne, Tara D Barwick, Eric O Aboagye, [18F]Fluciclatide PET as a biomarker of response to combination therapy of pazopanib and paclitaxel in platinum-resistant/refractory ovarian cancer, Eur. J. Nucl. Med. Mol. Imaging 47 (5) (2020) 1239–1251.

[36] Suraiya Dubash, Marianna Inglese, Francesco Mauri, Kasia Kozlowski, Pritesh Trivedi, Mubarik Arshad, Amarnath Challapalli, Tara Barwick, Adil Al-Nahhas, Rex Stanbridge, Conrad Lewanski, Matthew Berry, Frances Bowen, Eric O Aboagye, Spatial heterogeneity of radiolabeled choline positron emission tomography in tumors of patients with non-small cell lung cancer: first-in-patient

evaluation of [18F]fluoromethyl-(1,2-2H4)-choline, Theranostics 10 (19) (2020) 8677–8690.

[37] Shahriar Islam, Marianna Inglese, Matthew Grech-Sollars, Preetha Aravind, Suraiya Dubash, Tara D Barwick, Kevin O'Neill, James Wang, Azeem Saleem, James O'Callaghan, Giulio Anchini, Matthew Williams, Adam Waldman, Eric O Aboagye, Feasibility of [18F]fluoropivalate hybrid PET/MRI for imaging lower and higher grade glioma: a prospective first-in-patient pilot study, Eur. J. Nucl. Med. Mol. Imaging 50 (13) (2023) 3982–3995.

[38] Rohini Sharma, Marianna Inglese, Suraiya Dubash, Haonan Lu, David J Pinato, Chandan Sanghera, Neva Patel, Anthony Chung, Paul D Tait, Francesco Mauri, William R Crum, Tara D Barwick, Eric O Aboagye, Monitoring response to transarterial chemoembolization in hepatocellular carcinoma using 18F-fluorothymidine PET, J. Nucl. Med. 61 (12) (2020) 1743–1748.

[39] Paolo Zanotti-Fregonara, William C Kreisl, Robert B Innis, Chul Hyoung Lyoo, Automatic extraction of a reference region for the noninvasive quantification of translocator protein in brain using 11C-PBR28, J. Nucl. Med. 60 (7) (2019) 978–984.

[40] Krishna Kanta Ghosh, Parasuraman Padmanabhan, Chang-Tong Yang, Sachin Mishra, Christer Halldin, Balázs Gulyás, Dealing with PET radiometabolites, EJNMMI Res. 10 (1) (2020) 109.

[41] Tao Sun, Yaping Wu, Wei Wei, Fangfang Fu, Nan Meng, Hongzhao Chen, Xiaochen Li, Yan Bai, Zhenguo Wang, Jie Ding, Debin Hu, Chaojie Chen, Zhanli Hu, Dong Liang, Xin Liu, Hairong Zheng, Yongfeng Yang, Yun Zhou, Meiyun Wang, Motion correction and its impact on quantification in dynamic total-body 18F-fluorodeoxyglucose PET, EJNMMI Phys. 9 (1) (2022) 62.

[42] Felix P Kuhn, Geoffrey I Warnock, Cyrill Burger, Katharina Ledermann, Chantal Martin-Soelch, Alfred Buck, Comparison of PET template-based and MRI-based image processing in the quantitative analysis of C11-raclopride PET, EJNMMI Res. 4 (1) (2014) 7.

[43] M C F Cysouw, S V S Golla, V Frings, E F Smit, O S Hoekstra, G M Kramer, R Boellaard, QuIC-ConCePT Consortium, Partial-volume correction in dynamic PET-CT: effect on tumor kinetic parameter estimation and validation of simplified metrics, EJNMMI Res. 9 (1) (2019) 12.

[44] Chris W J van der Weijden, Pascalle Mossel, Anna L Bartels, Rudi A J O Dierckx, Gert Luurtsema, Adriaan A Lammertsma, Antoon T M Willemsen, Erik F J de Vries, Non-invasive kinetic modelling approaches for quantitative analysis of brain PET studies, Eur. J. Nucl. Med. Mol. Imaging 50 (6) (2023) 1636–1650.

[45] Sophia Attwells, Elaine Setiawan, Pablo M Rusjan, Cynthia Xu, Celeste Hutton, Dorsa Rafiei, Benjamin Varughese, Alan Kahn, Stephen J Kish, Neil Vasdev, Sylvain Houle, Jeffrey H Meyer, Translocator protein distribution volume predicts reduction of symptoms during open-label trial of celecoxib in major depressive disorder, Biol. Psychiatry 88 (8) (2020) 649–656.